ChemComm

COMMUNICATION

View Article Online
View Journal | View Issue

Cite this: *Chem. Commun.*, 2022, **58**, 6638

Received 25th January 2022,
Accepted 5th April 2022

DOI: 10.1039/d2cc00490a

rsc.li/chemcomm

Activating oxygen deficient TiO_2 in the visible region by Bi_2MoO_6 for CO_2 photoreduction to methanol†

Risov Das,[ab] Kousik Das,[ab] Sathyapal R. Churipard[ab] and Sebastian C. Peter*[ab]

Fast photogenerated charge recombination and inappropriate bandgap for visible light driven charge generation hinders the performance of TiO_2. In this study, TiO_2 was activated for visible light driven CO_2 reduction in the presence of Bi_2MoO_6 as an electron donor. Furthermore, the introduction of oxygen vacancies resulted in enhanced CO_2 adsorption and conversion. The best catalyst gives 27.1 μmol g^{-1} h^{-1} methanol formation. DRIFTS was used to explain the methanol formation mechanism on oxygen deficient TiO_2.

Rapid escalations in the demand for energy globally have set researchers on a quest to design and develop new energy production and storage technologies that can meet this demand sustainably. One such route is the use of abundantly available solar energy to convert anthropogenic CO_2 to energy. As an added benefit, this can also mitigate the greenhouse effects caused by the rise in CO_2 levels in the atmosphere.[1] Transition metal oxide-based semiconductors are considered to be promising photocatalysts due to their suitable band energy and excellent stability against photodegradation. For example, TiO_2,[2] WO_3,[3] Bi_2MoO_6,[4] $BiVO_4$[5] *etc.* have been extensively used for the photocatalytic hydrogen evolution reaction (HER) and CO_2 reduction reaction (CO_2RR).[6]

Despite having promising photocatalytic activity, the practical application of TiO_2 is constrained by its poor visible light activity and its tendency to undergo extensive electron–hole recombination, reducing the extent of photogenerated electrons (e^-) available for photoconversion. Similarly, Bi_2MoO_6, a promising visible light driven photocatalyst shows low quantum efficiency owing to its poor charge separation and slow carrier mobility.[7] Establishing a heterojunction between two semiconductors is an excellent strategy to significantly increase the photoconversion efficiency by not only modulating the light sensitivity towards the visible region but also promoting the charge carrier separation.[8] In addition, surface engineering leading to the generation of oxygen vacancies (O_v) can also increase the lifetime of photogenerated e^-s by creating trap states between the conduction and valence band.[9] Here, Bi_2MoO_6 is used as an e^- donor to activate TiO_2 under visible light. In addition, O_v was created deliberately to offer optimum CO_2 chemisorption opportunities at the TiO_2 surface. With the help of this dual strategy, we were able to achieve a dramatic increment of the CO_2RR performance by suppressing the drawbacks of the individual components. CH_3OH was obtained as the major product, which is regarded as a high energy dense fuel.[10]

TiO_2 and Bi_2MoO_6 and composites were synthesised by solvothermal processes. Pre-synthesized TiO_2 was added to an autoclave along with $Bi(NO_3)_3$ and Na_2MoO_4 to make a suitable interface between TiO_2 and Bi_2MoO_6 for facile e^- transfer within the heterojunction. The formation of the heterojunction is depicted *via* TEM and SEM images in Fig. 1a and b, which demonstrate the anchoring of Bi_2MoO_6 nano-seeds on TiO_2 nano ribbons. The HRTEM image in Fig. S1 (ESI†) depicts the (101) plane of TiO_2 and (131) plane of Bi_2MoO_6, which are in intimate contact with each other to form the heterostructure in the composite catalyst. The nano-seed like morphology of pristine Bi_2MoO_6 and the ribbon like morphology of pure TiO_2 were confirmed from EDX colour mapping which showed that the seed like morphology contains Bi, Mo and O (Fig. S2a–d, ESI†) and the ribbon like morphology mainly consists of Ti and O (Fig. S3a–d, ESI†). The ratio of Bi_2MoO_6 and TiO_2 was varied during the synthesis process to optimize the composite composition for best CO_2 photoreduction activity. The weight ratios of Bi_2MoO_6 and TiO_2 were varied from 3 : 1, to 2 : 1 and 1 : 1 and termed as **Bi3@Ti1**, **Bi2@Ti1** and **Bi1@Ti1**. Henceforth this nomenclature will be used throughout the manuscript. The PXRD patterns of the TiO_2, Bi_2MoO_6, and Bi_2MoO_6/TiO_2

---

[a] New Chemistry Unit, Jawaharlal Nehru Centre for Advanced Scientific Research, Jakkur, Bangalore-560064, India. E-mail: sebastiancp@jncasr.ac.in, sebastiancp@gmail.com

[b] School of Advanced Materials, Jawaharlal Nehru Centre for Advanced Scientific Research, Jakkur, Bangalore-560064, India

† Electronic supplementary information (ESI) available. See DOI: https://doi.org/10.1039/d2cc00490a

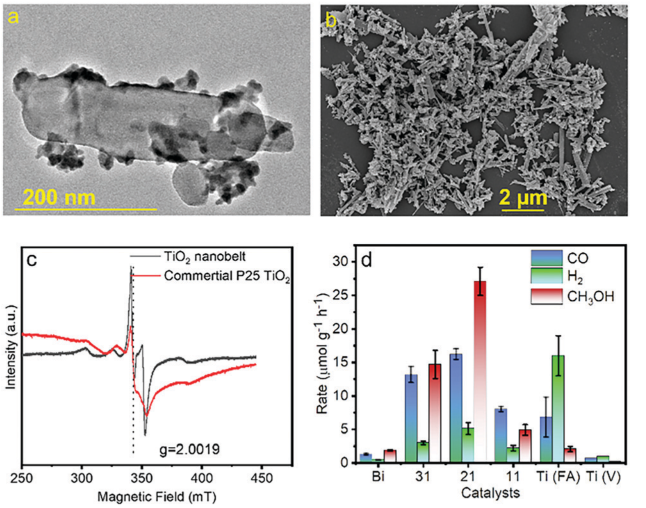

Fig. 1 Characterization and CO_2RR performance of Bi_2MoO_6/TiO_2 composites. (a) TEM and (b) SEM image of TiO_2 nanoribbon and Bi_2MoO_6 nanoparticle composite. (c) ESR spectra of as synthesised TiO_2 nanoribbon and commercially available P25 TiO_2 for qualitative understanding of O_v. (d) Comparison of the photocatalytic activity of all the catalysts after 6 h. Here Bi, 31, 21, 11 and Ti refers to Bi_2MoO_6, Bi3@Ti1, Bi2@Ti1, Bi1@Ti1 and TiO_2 respectively. (FA) means full arc contains UV-visible light and (V) means visible light illumination.

heterostructures are shown in Fig. S4a (ESI†). Six distinctive peaks observed for TiO_2 at $2\theta = 25.28°$ (101), 37.80° (004), 48.05° (200), 53.89° (105), 55.06° (211) and 62.69° (204) corroborate with anatase TiO_2 (*I*4$_1$/*amd)*.[11] In the case of Bi_2MoO_6, the diffraction peaks at 28.25°, 32.59°, 33.07°, 46.72°, 47.07°, 55.46°, 55.53° and 56.16° could be perfectly indexed to the (131), (002), (060), (202), (260), (331), (133) and (191) planes of orthorhombic Bi_2MoO_6 (*Pca*2$_1$).[12] For the Bi_2MoO_6/TiO_2 heterostructures, all of the peaks can be assigned to either TiO_2 or Bi_2MoO_6. The absence of extra peaks proves the formation of a pure heterojunction. The (101) plane of TiO_2 with very less intensity is observed in the XRD patterns of the composite, which is due to the lower diffraction ability of TiO_2 compared to Bi_2MoO_6. With an increase in the amount of TiO_2, the peak intensity also increases (Fig. S4a, ESI†). Instead of using commercially available TiO_2 (P25), here TiO_2 was treated with a base for increasing O_v in it. The presence of more O_v in the TiO_2 nano ribbons compared to P25 was understood from EPR spectroscopy (Fig. 1c). O_v induces the formation of Ti^{3+} along with Ti^{4+} ($Ti^{4+}O_2 \rightarrow Ti^{3+}Ti^{4+}O_{(2-x)} + X/2O_2$).

The presence of more Ti^{3+} compared to Ti^{4+} in the TiO_2 nanoribbons was depicted from X-ray photoelectron spectroscopy (XPS) in Fig. S5 (ESI†). The deconvoluted spectra of P25 also indicated the presence of Ti^{3+} although in much lower quantity compared to the TiO_2 nanoribbons. The $3d^1$ e^- in Ti^{3+} generates an EPR signal.[13] Hence, the more intense EPR signal of the TiO_2 nano ribbons compared to P25 clearly indicates the presence of more Ti^{3+} or more O_v in the TiO_2 nano ribbons. These O_v act as hole scavengers ($Ti^{3+} + h^+ \rightarrow Ti^{4+}$) and oxygen deficient TiO_2 lowers the CO_2 adsorption energy on the TiO_2 surface, which in turn facilitates the CO_2 reduction process (Fig. S4b, ESI†).[14] CO_2 Temperature Programmed Desorption (TPD) in Fig. S6 (ESI†) revealed that the TiO_2 with vacancies has better CO_2 uptake capacity (1.85 μmol g^{-1}) compared to pure TiO_2 (0.53 μmol g^{-1}) (Table S1, ESI†). The CO_2 photoreduction performance of all the catalysts was tested under solar simulated 450 W Xe light illumination in a sealed quartz tube. Methanol was obtained as the major product and CO as a minor product. The CO_2 reduction performance (rate of product formation) of all the catalysts is summarized in Fig. 1d and Table S2 (ESI†). Among all the composite catalysts, Bi2@Ti1 exhibited the best catalytic activity. It achieved a methanol formation rate of 27.1 μmol g^{-1} h^{-1} (Fig. S7, ESI†), which is better than most of the TiO_2 based catalysts reported for methanol (Table S3, ESI†). Interestingly, pristine TiO_2 produced more CO compared to methanol under UV-Visible light illumination. Upon switching the illuminated light from the UV-visible to visible region the activity reduced drastically as e^-s and holes cannot be generated by visible light (>400 nm) illumination on TiO_2 due to its large band gap. On the other hand, pristine Bi_2MoO_6 also could not perform satisfactorily due to fast charge recombination. In the composite material photogenerated e^-s of Bi_2MoO_6 were transferred to the neighbouring TiO_2 nano ribbons and activated TiO_2 for photocatalysis under visible light. The optimum supply of e^-s from Bi_2MoO_6 and the presence of O_v in TiO_2 for CO_2 adsorption and activation rendered Bi2@Ti1 the best catalyst for methanol formation. The presence of more Bi_2MoO_6 facilitates more e^- for the kinetically demanding methanol formation process ($6e^-$) in comparison to the production of CO ($2e^-$).[15] Therefore, better methanol formation rate was observed for Bi3@Ti1 compared to Bi1@Ti1 and pristine TiO_2. Furthermore, the role of each component of the CO_2 photoreduction reaction (CO_2RR) was confirmed from a series of control experiments. Finally, the CO_2RR was carried out with $^{13}CO_2$ and the obtained methanol and CO were examined by GCMS, which clearly shows the formation of ^{13}CO (Fig. S8a and c, ESI†) and $^{13}CH_3OH$ (Fig. S8b and d, ESI†) confirming that the generated products are solely coming from the CO_2RR. Cyclability of the spent catalyst showed an unaltered product formation rate for 6 consecutive cycles meaning that the catalyst is stable for repeated performance (Fig. S9, ESI†).

Photocatalytic CO_2RR in the absence of CO_2, light, catalyst and 0.1M NaOH solution showed neither gaseous nor any liquid product formation, indicating the crucial role played by these components. After 6 cycles the catalysts were examined *via* XRD (Fig. S10, ESI†), TEM (Fig. S11a, ESI†) and SEM (Fig. S11b, ESI†) analyses to understand the structural and morphological integrity. Post catalysis samples displayed similar XRD patterns, and morphology compared to the pristine catalyst. All the catalysts has produced some amount of H_2. However, upon composite formation with Bi_2MoO_6, the HER was suppressed dramatically compared to pristine TiO_2. Therefore, it can be inferred that Bi2@Ti1 not only performed better towards CO_2 reduction but also suppressed the e^- wasting competitive HER, which is considered as one of the biggest challenges in photocatalytic CO_2RR. Improved activity of

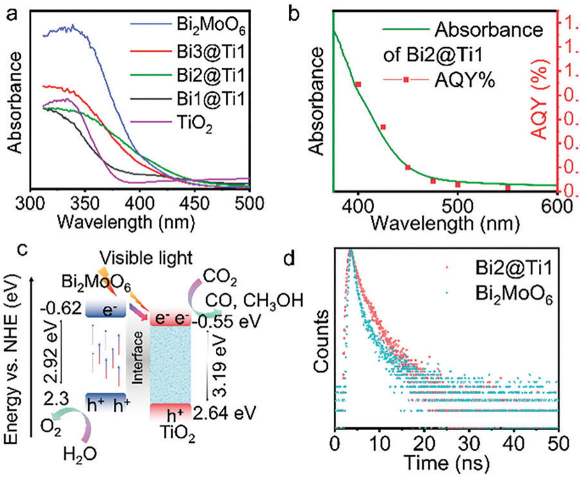

Fig. 2 Band structure and charge transfer process. (a) UV-DRS spectra of all the composites and pristine individuals. (b) Comparison of absorbance and AQY% to check the co-relation between absorbance and activity of Bi2@Ti1 catalyst. (c) Electron transfer route in Bi_2MoO_6/TiO_2 composite catalysts *via* type-II mechanism. (d) Time dependent photoluminescence spectra of pure Bi_2MoO_6 and Bi2@Ti1.

composites and the role of Bi_2MoO_6 as an e^- donor can be understood by the analysis of the band structure and charge transfer process. As depicted in Fig. 2a, the absorbance spectra revealed that TiO_2 can only harvest the UV part of the solar spectrum. Therefore, TiO_2 could not perform under visible light illumination. On the other hand, Bi_2MoO_6 has an absorption edge in the visible region. Therefore, the composite materials have UV as well as visible light absorption capability. The agreement between the absorption onset of Bi2@Ti1 and overall apparent quantum yield (AQY%) was understood upon different wavelength chopped light illumination (Fig. 2b). The CO_2 reduction process terminated at more than 475 nm light irradiation and the AQY% trends followed the Bi2@Ti1 absorption pattern meaning that the photocatalysis proceeded *via* excited e^-s of Bi_2MoO_6. Therefore, the highest AQY of 0.89% was obtained by 400 ± 10 nm light irradiation where Bi_2MoO_6 shows maximum absorption.

Further insight of e^- transfer was understood by band gap calculation through a Tauc plot (Fig. S12, ESI†) and band alignment calculation by Mott–Schottky measurements. It showed that TiO_2 and Bi_2MoO_6 have bandgaps of 3.19 eV and 2.92 eV, respectively. From the Mott–Schottky measurements it can be said that both the semiconductors are n-type and hence their conduction band maxima (CBM) stay near to the Fermi level. Therefore, the CBM position was obtained by adding −0.1 V with the flat band potential (V_{fb}) obtained from Mott–Schottky plots (Fig S13a and b, ESI†). As depicted in Fig. 2c the CBM positions of Bi_2MoO_6 and TiO_2 are situated at −0.71 V and −0.58 V. Therefore, the excited e^-s of Bi_2MoO_6 can easily be transferred to TiO_2 upon visible light irradiation, which can further be used for the CO_2RR. Fig. 2c clearly shows that TiO_2 has enough potential for CO_2 to methanol or CO production by utilizing excited e^-s of Bi_2MoO_6 because −0.36 V and −0.54 V is the CO_2 to methanol and CO formation potential, respectively. Therefore, the leftover photogenerated holes in the valence band of Bi_2MoO_6 participated in the water oxidation reaction. The evolved O_2 was quantified by gas chromatography (GC) which showed that the amount of evolved O_2 is approximately matching with the stoichiometric amount (Fig. S14, ESI†). The valence band positions were determined using band gap value and CBM position. Time dependent photoluminescence study further elucidated the e^- transfer pathway. Fig. 2d and Table S4 (ESI†) show that the pristine Bi_2MoO_6 had lower lifetime for the excited electrons (τ_{avg} = 2.2 ns) compared to Bi2@Ti1 (τ_{avg} = 2.7 ns). On the other hand, as shown in Fig. S15 (ESI†) static photo luminescence (PL) study showed that the composites have weaker PL intensities compared to pristine Bi_2MoO_6. This manifests that the excited e^-s of pristine Bi_2MoO_6 quickly recombine with photogenerated holes, whereas in the composites the e^- goes to neighbouring TiO_2 instead of recombining. Therefore, the composites showed less PL intensity and more excited charge lifetime.[16] Photoelectrochemical measurements including interfacial charge transfer resistance and light induce current generation capacity were understood from electrochemical impedance spectroscopy (Fig. S16a, ESI†) and transient photocurrent measurements (Fig. S16b, ESI†). Interestingly, Bi2@Ti1 has the least and pristine Bi_2MoO_6 has the highest charge transfer resistance. An interesting photocurrent generation feature was seen for TiO_2 and the composites. TiO_2 showed rapid photocurrent decay compared to the composites upon light off (Fig. S17, ESI†). Moreover, Bi2@Ti1 exhibited the highest photocurrent. Pristine TiO_2 has delivered no extra current under visible light illumination. The featured photocurrent for TiO_2 in Fig. S16b (ESI†) is due to UV-visible light irradiation. Pristine Bi_2MoO_6 has much less photocurrent production ability and high charge transfer resistance. Therefore, its performance as a photocatalyst is lacking. However, upon composite formation these drawbacks were overcome and the CO_2RR performance increased.

The methanol formation pathway was understood from the identification of intermediates formed during CO_2 hydrogenation *via* operando DRIFTS (Fig. 3a). The peaks observed at 1372 cm^{-1} and 1583 cm^{-1} represent the bidentate and monodentate carbonates generated *via* adsorption of CO_2 in the O_v–TiO_2 surface.[17] Most importantly, the intensity of the band at 1655 cm^{-1} corresponding to *COOH has increased with light irradiation time.[18] The *COOH intermediate is regarded as the first and most common intermediate for CO_2 hydrogenation.[18]

A tiny peak evolution at 2095 cm^{-1} corresponding to the *CO intermediate was also found, which upon desorption from the surface can produce gaseous CO.[18] The most important intermediates of methanol formation are $*OCH_3$ and *CHO. A monotonous evolution of the IR peaks at 1036 cm^{-1} and 1114 cm^{-1} implicitly indicates the presence of these 2 important intermediates.[5] The *CO intermediate was rapidly converted to the *CHO intermediate; therefore, the intensity of the *CO intermediate remained negligible. On the other hand, the $*OCH_3$ intermediate showed a prominent peak. Therefore, it can be inferred that the $*OCH_3$ intermediate has chemisorbed on the O_v–TiO_2 surface for longer time and got protonated on

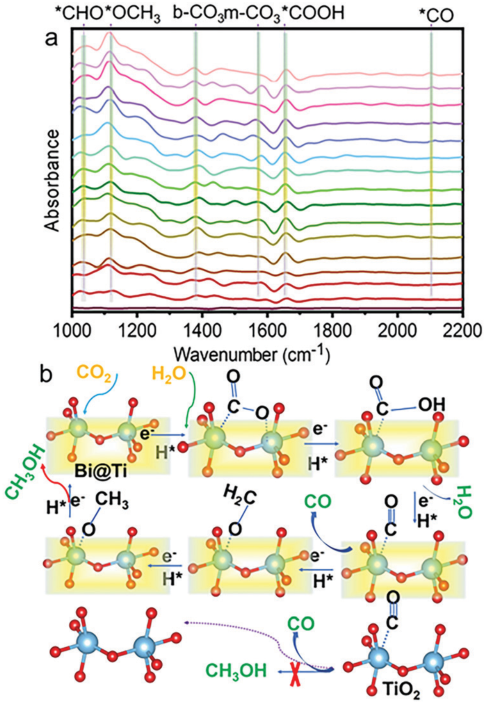

Fig. 3 *In situ* study for understanding the methanol formation mechanism. (a) Operando DRIFTS with CO_2 and water vapour under 450 W Xe light illumination with the Bi2@Ti1 catalyst. (b) Plausible methanol formation mechanism on the O_v–TiO_2 surface. It also shows without Bi_2MoO_6, CH_3OH formation became difficult.

the O site for methanol formation.[19] The absence of methane eliminates the probability of proton adsorption on the C centre of the $*OCH_3$ intermediate (Fig. S18, ESI†). Based on the knowledge of these intermediates, the formate mechanism for methanol formation can be confirmed. A mechanistic scheme for methanol formation *via* a 6 proton coupled e^- transfer process is shown in Fig. 3b. CO and H_2O were obtained as the by-products through this mechanism. Upon $*OCH_3$ protonation, the catalyst bed can be regenerated without any chemical corrosion. Moreover, as mentioned previously, the formed heterojunction allows TiO_2 to utilize visible light energy more effectively *via* additional photo-generated e^- transfer from Bi_2MoO_6 for the reaction, whereby the yield of methanol formation is greatly enhanced.

In summary, introducing Bi_2MoO_6 nanoparticles into O_v TiO_2 allows e^- transfer through the intimate interface. Thereby, the active sites of TiO_2 were used for CO_2 adsorption and photogenerated charges of Bi_2MoO_6 were used for the CO_2RR. A series of photophysical and photoelectrochemical studies established the regions of best activity in the Bi2@Ti1 catalyst. Finally, the methanol formation mechanism was predicted based on the intermediate's information from operando DRIFTS. Further modification of the reaction conditions can lead to better increment of the performance and can be used for large scale application owing to the high durability of this composite.

Financial support from the Department of Science and Technology (DST) (DST/TMD/(EWO)/IC#5-2018/02) is gratefully acknowledged. SCP thanks DST for the SwarnaJayanti Fellowship (DST/SJF/CSA-02/2017-18). RD, KD and SRC thank CSIR and JNCASR for the research fellowships.

Conflicts of interest

There are no conflicts to declare.

Notes and references

1 (*a*) W. Tu, Y. Zhou and Z. Zou, *Adv. Mater.*, 2014, **26**, 4607–4626; (*b*) S. Roy, A. Cherevotan and S. C. Peter, *ACS Energy Lett.*, 2018, **3**, 1938–1966; (*c*) S. C. Peter, *ACS Energy Lett.*, 2018, **3**, 1557–1561; (*d*) W. Zhou, Q. Xie, J. Li, C. Zhengwei and F. Peng, *Bull. Mater. Sci.*, 2019, **42**, 12; (*e*) D.-H. Lan, Y.-X. Gong, N.-Y. Tan, S.-S. Wu, J. Shen, K.-C. Yao, B. Yi, C.-T. Au and S.-F. Yin, *Carbon*, 2018, **127**, 245–254.

2 R. Das, S. Chakraborty and S. C. Peter, *ACS Energy Lett.*, 2021, **6**, 3270–3274.

3 L. J. Zhang, S. Li, B. K. Liu, D. J. Wang and T. F. Xie, *ACS Catal.*, 2014, **4**, 3724–3729.

4 R. Das, K. Das, B. Ray, C. P. Vinod and S. C. Peter, *Energy Environ. Sci.*, 2022, DOI: **10.1039/D1EE02976B**.

5 R. Das, S. Sarkar, R. Kumar, S. D. Ramarao, A. Cherevotan, M. Jasil, C. P. Vinod, A. K. Singh and S. C. Peter, *ACS Catal.*, 2022, **12**, 687–697.

6 J.-K. G. Wei Zhou, S. Shen, J. Pan, J. Tang, L. Chen, C.-T. Au and S.-F. Yin, *Acta Phys. -Chim. Sin.*, 2020, **36**, 1906048.

7 H. Yu, L. Jiang, H. Wang, B. Huang, X. Yuan, J. Huang, J. Zhang and G. Zeng, *Small*, 2019, **15**, 1901008.

8 (*a*) L. Etgar, P. Gao, Z. Xue, Q. Peng, A. K. Chandiran, B. Liu, M. K. Nazeeruddin and M. Grätzel, *J. Am. Chem. Soc.*, 2012, **134**, 17396–17399; (*b*) R. Hao, G. Wang, H. Tang, L. Sun, C. Xu and D. Han, *Appl. Catal., B*, 2016, **187**, 47–58; (*c*) E. Vesali-Kermani, A. Habibi-Yangjeh, H. Diarmand-Khalilabad and S. Ghosh, *J. Colloid Interface Sci.*, 2020, **563**, 81–91.

9 (*a*) Y. Zhang, Z. Xu, G. Li, X. Huang, W. Hao and Y. Bi, *Angew. Chem., Int. Ed.*, 2019, **58**, 14229–14233; (*b*) Y. Fang, Z. Liu, J. Han, Z. Jin, Y. Han, F. Wang, Y. Niu, Y. Wu and Y. Xu, *Adv. Energy Mater.*, 2019, **9**, 1803406.

10 (*a*) A. Cherevotan, J. Raj, L. Dheer, S. Roy, S. Sarkar, R. Das, C. P. Vinod, S. Xu, P. Wells, U. V. Waghmare and S. C. Peter, *ACS Energy Lett.*, 2021, **6**, 509–516; (*b*) D. Bagchi, J. Raj, A. K. Singh, A. Cherevotan, S. Roy, K. S. Manoj, C. P. Vinod and S. C. Peter, *Adv. Mater.*, 2022, 2109426.

11 H. G. Yang, C. H. Sun, S. Z. Qiao, J. Zou, G. Liu, S. C. Smith, H. M. Cheng and G. Q. Lu, *Nature*, 2008, **453**, 638–641.

12 Z. Jia, F. Lyu, L. C. Zhang, S. Zeng, S. X. Liang, Y. Y. Li and J. Lu, *Sci. Rep.*, 2019, **9**, 7636.

13 X. Pan, M.-Q. Yang, X. Fu, N. Zhang and Y.-J. Xu, *Nanoscale*, 2013, **5**, 3601–3614.

14 (*a*) W. Pipornpong, R. Wanbayor and V. Ruangpornvisuti, *Appl. Surf. Sci.*, 2011, **257**, 10322–10328; (*b*) J.-B. Pan, B.-H. Wang, J.-B. Wang, H.-Z. Ding, W. Zhou, X. Liu, J.-R. Zhang, S. Shen, J.-K. Guo, L. Chen, C.-T. Au, L.-L. Jiang and S.-F. Yin, *Angew. Chem., Int. Ed.*, 2021, **60**, 1433–1440.

15 Y. Fang and X. Wang, *Chem. Commun.*, 2018, **54**, 5674–5687.

16 Y. P. Xie, Y. Yang, G. Wang and G. Liu, *J. Colloid Interface Sci.*, 2017, **503**, 198–204.

17 T. H. Tan, B. Xie, Y. H. Ng, S. F. B. Abdullah, H. Y. M. Tang, N. Bedford, R. A. Taylor, K.-F. Aguey-Zinsou, R. Amal and J. Scott, *Nat. Catal.*, 2020, **3**, 1034–1043.

18 X. Li, Y. Sun, J. Xu, Y. Shao, J. Wu, X. Xu, Y. Pan, H. Ju, J. Zhu and Y. Xie, *Nat. Energy*, 2019, **4**, 690–699.

19 Z. Sun, T. Ma, H. Tao, Q. Fan and B. Han, *Chem*, 2017, **3**, 560–587.